ASME Journal of Mechanical Design
Online journal at:
https://asmedigitalcollection.asme.org/mechanicaldesign

Flexure Hinge Design and Optimization for Compact Anthropomorphic Grippers Made via Metal Additive Manufacturing

Martin Tschiersky[1]
Chair of Precision Engineering,
University of Twente,
Enschede 7500 AE, The Netherlands
e-mail: m.tschiersky@utwente.nl

Jan J. de Jong
Chair of Precision Engineering,
University of Twente,
Enschede 7500 AE, The Netherlands
e-mail: j.j.dejong@utwente.nl

Dannis M. Brouwer
Chair of Precision Engineering,
University of Twente,
Enschede, 7500 AE, The Netherlands
e-mail: d.m.brouwer@utwente.nl

Flexure-based grippers offer an attractive alternative to conventional grippers used in robotics and automation. However, most existing designs appear to suffer from insufficient range of motion, loadability, and support stiffness. This article presents an approach to obtain well-performing flexure hinges for compact anthropomorphic grippers made via metal additive manufacturing. We propose a flexure hinge architecture that achieves a high range of motion despite the challenging combination of a small design space, high Young's modulus, and limited minimum feature size. Furthermore, we present an optimization procedure to generate suitable tendon-driven designs with high loadability. Using this framework, a flexure hinge with an outer diameter of 21.5 mm and range of motion of ±30 deg is synthesized. For the range of 0–30 deg, simulations show a lateral loadability of 52.5–18.6 N and lateral support stiffness of 12,309–11,130 N/m, determined at a gripper interface located 41.2 mm from the hinge pivot axis. Experiments confirm a loadability of at least 15.4 N and determined a stiffness of 8982 to 9727 N/m for same conditions. The results show that the flexure hinge architecture has large potential for a wide range of applications, while in combination with the optimization procedure, superior designs for tendon-driven grippers can be obtained. [DOI: 10.1115/1.4063362]

Keywords: compliant mechanism synthesis, compliant mechanisms, conceptual design, design evaluation, design for manufacturing, design of innovative devices, design of machine elements, design optimization, design theory and methodology

1 Introduction

Robot grippers are an essential component in the field of robotics and automation. They are involved in many automated handling processes, and their performance often determines the achievable handling time [1]. As one of the largest manufacturing sectors, the modern food industry still relies heavily on human labor to perform repetitive manual handling tasks, such as harvesting as well as pick and place operations [2–4]. Over the past decades, increasing efforts were made to automate these processes through the use of robots [2–4]. To this end, suitable grippers for handling food products such as fruits, vegetables, meat, poultry, and fish are crucial.

Impactive grippers are the most frequently used type in food handling [3] and the most common type overall [5]. They work by exerting mechanical forces against the external surface of the grasped object [5]. A large variety of impactive grippers has been devised in the past [5–10], of which anthropomorphic grippers form a prominent subcategory. Anthropomorphic grippers feature three to five fingers, and their structure resembles that of a human hand [5]. The employed fingers can be either jointed or jointless [5].

Jointed fingers are traditionally designed as serial linkages using rigid links and conventional revolute joints, often actuated via tendons or additional links [5]. Grippers with jointed fingers can adapt to the size and shape of the grasped object and allow for performing various types of grasps. These grasps can be subdivided into force mating precision grasps (force-fit) in which the object is retained solely by means of friction, and contour matching power grasps (form-fit) in which the fingers embrace the object [1,5,11]. Jointless fingers are made from soft and flexible materials that cause the entire fingers to deform elastically. They typically exert less contact pressure on the grasped object [12]. However, their achievable prehension force and load-carrying capacity are comparatively lower [5], and their response time is generally slow [12]. Moreover, due to the lack of a well-defined kinematic structure and strong interactions with the grasped object precise control is difficult [1,5,12].

A potential way to improve on the design of jointed finger grippers is the use of flexible joints, i.e., flexures. Compared to conventional joints, such as bushings and bearings, which work through sliding or rolling contact between solid bodies, flexures obtain motion through elastic deformation of their deformable members [13]. As flexures feature no backlash, no friction, and low hysteresis, they facilitate simple, robust, and precise control. In addition, their force transparent characteristic enables self-sensing [14,15] and minimal remote sensing [16]. Due to the lack of relative motion between contacting surfaces, flexures require no lubrication, feature virtually no wear, and produce no polluting debris [13,17–21]. This makes flexure-based grippers not only suitable for vacuum and cryogenic conditions [17] but also suitable for handling food either when high hygiene standards are required or when used in wet and dirty environments [22]. By reducing the number of parts, flexure-based grippers can enable lightweight designs and low-cost production [23,24]. To this end, the use of monolithic structures in combination with additive manufacturing shows large potential [25–28].

[1]Corresponding author.

Contributed by the Mechanisms and Robotics Committee of ASME for publication in the Journal of Mechanical Design. Manuscript received June 2, 2023; final manuscript received August 21, 2023; published online October 6, 2023. Assoc. Editor: Yan Chen.

However, compared to conventional joints, flexures generally perform worse in terms of achievable range of motion, loadability, and support stiffness. Many flexure-based anthropomorphic fingers and grippers—often intended as prostheses—have been designed in the past [22–35]. Still, clear guidance on how to obtain a well-performing design with high loadability is missing, and authors often report poor stiffness properties in support directions. Previous research from our research group aimed at optimizing the loadability and support stiffness of flexure hinges for use in prosthetic fingers [36,37]. Yet, the resulting grippers turned out to be large and lacked sufficient load-carrying capacity. With the exception of the work of Martin and Robert [35], all of the earlier cited studies used plastics or elastomers as the flexure material, leaving the use of other materials largely unexplored.

This article proposes a compact flexure hinge design for use in human-sized anthropomorphic grippers. The design aims to provide a high loadability while having a suitable range of motion and sufficient support stiffness. To this end, a new flexure hinge architecture and dedicated optimization procedure are developed. Following this introduction, the flexure hinge architecture, computational models, and applied optimization procedure are described in Sec. 2. It is followed by Sec. 3, which presents a test specimen and test setup, and describes the physical verification. Subsequently, the computational and experimental results are presented and discussed in Secs. 4 and 5, respectively. Finally, Sec. 6 recapitulates the main findings of this article.

2 Methods

2.1 Specifications. The flexure hinges presented in this article are intended to be used as revolute finger joints in human-sized, tendon-driven anthropomorphic grippers. For this study, the joint that corresponds to the proximal interphalangeal (PIP) joint of a human index finger is chosen as a representative example. Figure 1 shows a schematic of the gripper finger topology along with the geometric parameters and the applied loads. To acquire the most design freedom while still maintaining human size, the size constraints are derived from the anthropomorphic data of a 99th percentile large man [38]. According to this, we determine that the joints' outer perimeter should not exceed an diameter of $D_o = 23$ mm, while the width is set to $w = 20$ mm. Based on studies on the functional range of motion of human finger joints [39,40], it is determined that a range of motion of ±30 deg is sufficient to carry out most relevant grasping tasks. The effective range of the angle γ between the intermediate phalanx and the proximal phalanx can be shifted by choosing the initial angle γ_{init} at which the flexure joint is in its neutral undeflected position, e.g., to the interval $\gamma = [25\ldots85]$ deg. To acquire designs for other joints, parameters D_o and w as well as the range of motion can be adjusted accordingly.

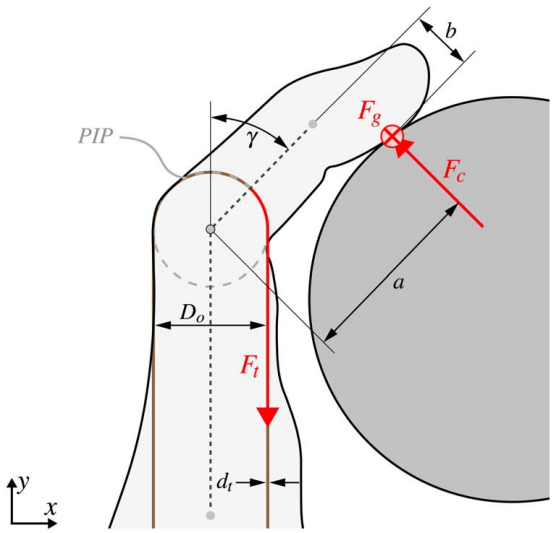

Fig. 1 Schematic load case for the PIP joint. The gripper finger and an arbitrary grasped object are drawn. The position of the PIP joint is indicated by a gray dashed circle with a gray dot at the center. Black dotted lines indicate the orientations of the intermediate and proximal phalanges. A solid line depicts the tendon to actuate the PIP joint. Arrows indicate the external forces acting on the finger. Relevant geometric parameters are presented in black. The vector of gravity acts along the width direction (z-direction), perpendicular to the drawn *x-y* plane. The corresponding force F_g is denoted by the ⊗ symbol. Its location coincides with the position of the contact point between finger and object.

In order to meet the requirements of the food industry, specifically with regards to hygiene and to achieve high performance, we propose the use of a monolithic structure made from a food-grade metal alloy via a conventional additive manufacturing process, namely, selective laser melting (SLM). Reductive manufacturing methods, such as electrical discharge machining, are deemed less suitable as they are anticipated to require additional assembly. While SLM offers large design freedom in terms of the achievable complexity, it also limits the amount of available materials and imposes challenging manufacturing constraints.

As the material, a performance grade Ti-6Al-4V is chosen. It is a biocompatible and highly corrosion-resistant titanium alloy that is widely used in metal additive manufacturing. It has a density of $\rho \approx 4390$ kg/m^3, a Young's modulus of $E = 110$ GPa, a yield strength of $\sigma_y > 900$ MPa, and a tensile strength of $\sigma_t > 980$ MPa [41]. Based on the model by Bartsch et al. [42], a Poisson's ratio of $\nu = 0.2919$ is used.

With regard to manufacturing constraints, the minimum producible wall thickness presents the most significant restriction in the scope of this work. Although previous studies found that walls as thin as 0.1 mm can be manufactured [43], design guidelines for Ti-6Al-4V generally recommend wall thicknesses ≥0.4 mm [44,45]. For this study, we determined, based on preliminary experiments, that a flexure thickness of ≥0.3 mm can be reliably produced by commercial suppliers. In addition, overhang angles are limited to 45 deg to avoid the use of support structures.

2.2 Load Case. The primary function of the flexure hinge is to allow for sufficient rotation in the degree-of-freedom, while providing maximal support for external loads acting on the finger. To this end, a static load case is investigated that corresponds to a precision grasp during which the finger is oriented parallel to ground. This grasp is chosen as it provides a clearly defined load case, since each finger only has a single contact with the grasped object. To model this load case, the flexure hinge is first deflected by an angle θ via a tendon. Subsequently, the tendon is fixed and an external load is applied to a contact point at the tip of the finger.

The applied external load F_{ext} at this contact point is the resultant of two force vectors. The first force vector corresponds to the contact force F_c between the finger and the grasped object. It acts within the *x-y* plane and maintains an orientation perpendicular to the intermediate phalanx. The second force vector corresponds to the force F_g exerted by the weight of the grasped object. It acts perpendicular to the *x-y* plane. The minimum magnitude of the contact force necessary to prevent the grasped object from slipping can be calculated as follows:

$$F_c = \frac{F_g}{\mu} \tag{1}$$

$$F_g = m\,g \tag{2}$$

where μ is the friction coefficient between the finger and the object, m is the mass of the object, and g is the gravitational acceleration. The magnitude of the total resultant external load vector for which support shall be maximized is

$$F_{\text{ext}} = \sqrt{F_c^2 + F_g^2} = m\,g\,\sqrt{1 + \frac{1}{\mu^2}} \tag{3}$$

and has a fixed angle of

$$\varphi = \arctan(\mu) \tag{4}$$

toward the x-y plane.

The contact point is assumed at a position, which is at a distance $a = 40$ mm in distal direction from the joint center along the intermediate phalanx and $b = 10$ mm perpendicular to it. The distances a and b effectively act as the levers for the forces F_c and F_g, causing an additional moment load on the joint. In order to counteract the moment in the rotational degree-of-freedom of the hinge caused by the contact force F_c and to maintain static equilibrium, the tendon exerts an additional force F_t onto the joint. The force acts along the tendon, which runs parallel to the proximal phalanx and is located at a distance of $\frac{D_o + d_t}{2}$ from the joint center, d_t being the diameter of the tendon.

2.3 Flexure Hinge Design. Using metal additive manufacturing to produce small-scale flexure hinges with a large range of motion is a challenging task. Due to the relatively high Young's modulus of metals in combination with the limitations regarding the minimum producible wall thickness set by the additive manufacturing process, the flexible members in common flexure hinge designs quickly exceed the admissible bending stress when the hinge undergoes large rotations. To mitigate this, we developed a new flexure hinge architecture which is a generalization and extension of the butterfly flexure pivot [17] concept. It describes a family of flexure hinges, which includes the previously known cartwheel hinge [19] as well as the butterfly flexure pivot itself. This architecture can be used to distribute bending deformations across multiple flexible members. Thereby, we aim to obtain flexure hinges that retain a high load capacity and sufficient support stiffness throughout a large range of motion and furthermore exhibit only small drift of their rotation axes.

The basic building block of this architecture is the leaf-type isosceles trapezoidal flexure pivot described in Refs. [46,47] and shown in Figs. 2(*a*) and 2(*b*). A leaf-type flexure pivot consists of two leafspring flexures and two rigid bodies, of which one is considered the mobile shuttle and the other being fixed. In its idealized description, it features a single rotational degree-of-freedom, which is a rotation of the shuttle about the axis at which the neutral planes of the two leafspring flexures intersect. In an isosceles trapezoidal flexure pivot, this intersection line always lies beyond the physical length of the flexures, resulting in a motion about a remote axis of rotation. This makes it possible to combine multiple flexure pivots that share a common axis of rotation into a single mechanism without interfering with another [46,47]. Like in the butterfly flexure pivot, this is used to construct flexure hinges in which multiple flexure pivots with collocated rotation axes are arranged in series, whereby each flexure pivot is only subject to a fraction of the total imposed rotation.

Every flexure pivot used in this architecture is symmetric about the vertical plane (see Fig. 2). All employed leafspring flexures have the same length l, thickness t, and distance from the initial pivot axis, causing in their ends to lie on the same inner and outer pitch diameter, d and D, respectively. Conceptually, the only geometric difference between the individual flexure pivots is the relative angle α between their flexures. However, two topological types can be distinguished based on whether the shuttle corresponds to the shorter base of the isosceles trapezoid at the center of the mechanism, type 1 shown in Fig. 2(*a*), or to the longer base along its perimeter, type 2 shown in Fig. 2(*b*).

The procedure to construct a flexure hinge following the architecture is as follows: Starting from a fixed frame of reference, a number n of flexure pivots with increasing angle $\alpha \leq \pi$ is stacked in series to form the first half of the hinge, alternating between types 1 and 2. This is shown in Fig. 2(*c*) for $n = 2$. Using a number $n \geq 2$, this results in flexure pivots of type 1 and 2 forming pairs of geometrically similar flexure pivots in which the shuttle of the first serves as the base of the second. This double compound flexure pivot in itself forms another fundamental building block of this architecture. Subsequently, the entire structure is mirrored about the horizontal symmetry plane (at $\alpha = \pi$), and the most outer flexure pivots of each symmetry half are connected to each other via a rigid body that occupies the center of the mechanism, as shown in Fig. 2(*d*). This way flexure hinges for any number of $n \geq 1$ can be synthesized, whereby $n = 1$ corresponds to a cartwheel hinge, $n = 2$ corresponds to a butterfly flexure pivot, and all $n > 3$ can be regarded as series configurations of the two. A schematic overview over all design configurations $n \leq 8$ is shown in Fig. 3.

2.4 Parametrization. The design of every flexure hinge based on the architecture presented in this article can be described using the parameters shown in Fig. 2. For each flexure pivot comprised in the flexure hinge, an angle α_i is used to describe the relative angle between its two flexures. Thereby, the angular positions of all flexures from the innermost ($i = 1$) until the outermost ($i = n$) flexure pivot in each hinge half are determined. Their radial positions and length l can be inferred from an inner pitch diameter d and outer pitch diameter D, and their thickness is given by t. The value of D is chosen according to the specifications, leaving a vector $\mathbf{x}$ of $n + 2$ design variables to be optimized:

$$\mathbf{x} = [\alpha_1, \ldots, \alpha_n, d, t] \tag{5}$$

For consistency, all flexure hinge mechanisms presented in this article use a pitch diameter $D = 20$ mm and width $w = 20$ mm.

2.5 Simulation. To analyze different flexure hinge designs during optimization, the flexible multibody dynamics software package SPACAR [48] is used to perform static simulations. A two-dimensional representation of the simulation procedure is shown in Fig. 4.

The entire mechanism, which encompasses the flexure hinge as well as additional components to apply the loads, is built using

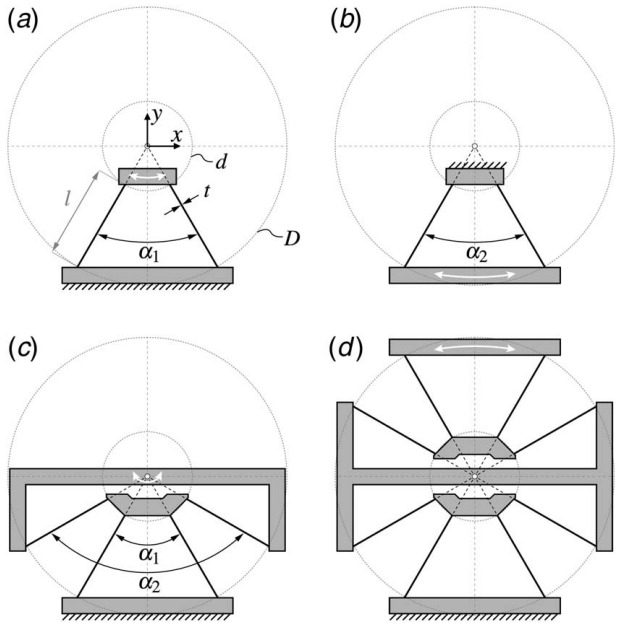

Fig. 2 Building blocks and fundamental synthesis steps. (*a*) flexure pivot type 1, (*b*) flexure pivot type 2, (*c*) two pivots, type 1 and 2, stacked in series to create a double compound flexure pivot, (*d*) the mirroring operation to create a butterfly flexure pivot from two double compound flexure pivots. Explicit parameters are drawn in black. Implicit parameters are drawn in gray. White arrows indicate the shuttle motion. The Cartesian coordinate system used for design and simulation is shown in (*a*).

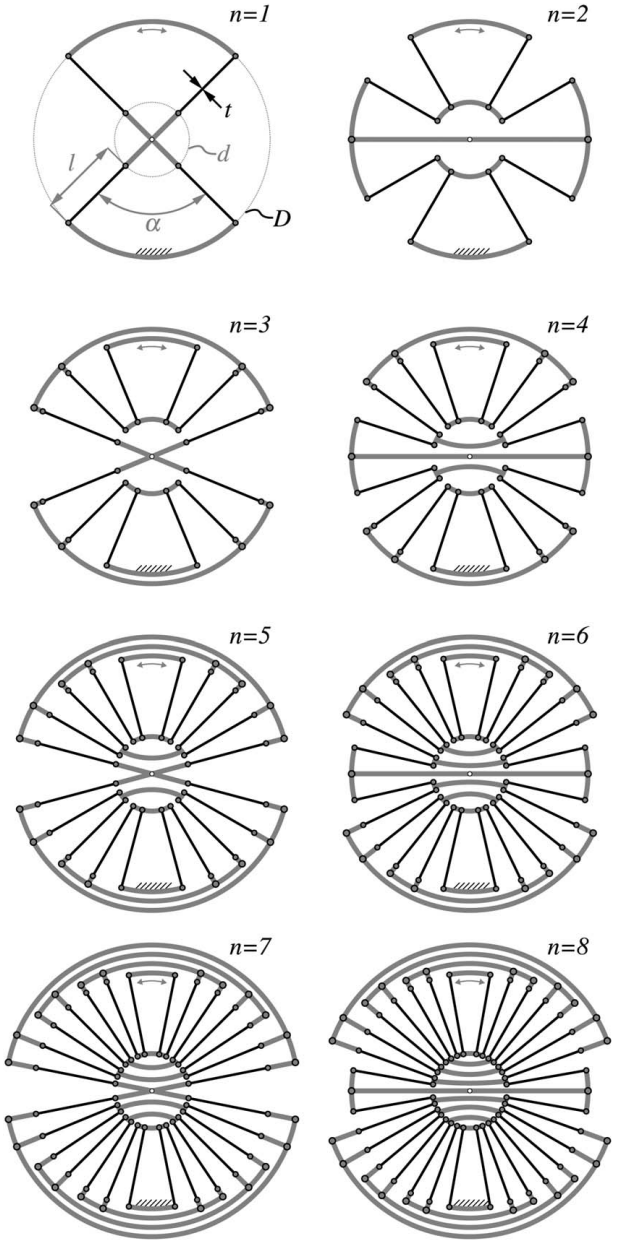

Fig. 3 Flexure hinge configurations for $n = [1…8]$ using the "default" design, including a cartwheel hinge ($n = 1$) and a butterfly flexure pivot ($n = 2$). Flexures are drawn in black and intermediate bodies in gray. Selectable parameters are shown in black and resulting ones gray.

finite two-node beam elements. These beam elements use six discrete deformation modes to express their elastic behavior. The hinges are modeled similar to the depictions in Fig. 3, whereby flexible beam elements are used for the flexures and rigid beam elements for the intermediate bodies. In addition to the hinge itself, a rigid lever with a small extension and a ring segment are connected to the mobile shuttle of the hinge in order to apply the loads as specified in Sec. 2.2. The lever extends from the top shuttle to the load application point assuming an initial joint orientation of $\gamma_{\text{init}} = 0$, such that γ as shown in Fig. 1 equals the joint angle θ. The ring segment that connects to the lever extends along the outer perimeter of the joint at a radius $\frac{D_o + d_t}{2}$ from the hinge center and ends at the angular position θ.

The simulation is conducted in two steps. During the first step, the rotation angle θ is applied to the hinge by moving the beam

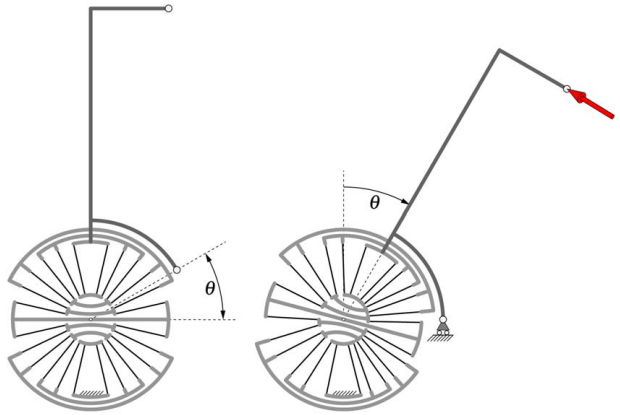

Fig. 4 Optimization model. The left subfigure shows the undeformed state before any loads are applied. The right subfigure depicts the two-step loading procedure. In the first step, the free node at the end of the ring segment is moved and fixed to the horizontal axis, representing the load by a tendon pulling at the phalanx and applying a rotation θ ($= 31$ deg). In the second step, the external force F_{ext}, representing the combined interaction forces between gripper finger and object, is applied at the end of the load lever. The force F_{ext} is indicated by the perspective arrow and has a fixed angle φ ($= 26.57$ deg) toward the drawn x-y plane.

node at the ring segment's free end to the horizontal axis ($y = 0$). Thereby, the node is fixed to that height but is still free to move along the horizontal (x) and out-of-plane (z) axes as well as to rotate about all axes. The resulting load on the flexure hinge is equivalent to actuating the hinge by a tendon that is fixed to the top lever and runs on top of a cylinder surface with diameter D_o. In the second step, an external load force F_{ext} is applied at the load application point, which is located at the end of the small extension from the lever. While applying the load, the external load force vector has a fixed orientation with respect to the lever, pointing perpendicular at it while maintaining the angle φ toward the mechanism (x-y) plane. Thus, the two-step simulation emulates the loads that occur during a precision grasp as described in Sec. 2.2.

2.6 Optimization. The objective of the optimization is to maximize the external force F_{ext}, which the flexure hinge can endure after being deflected by an angle θ that corresponds to its maximum range of motion, adding a safety margin of 1 deg. To this end, the flexure hinge is deflected to $\theta = 31$ deg, and F_{ext} is increased in simulation until the von Mises stress σ_{mises} in any of the flexures reaches the stress limit

$$\sigma_{\text{lim}} = \frac{\sigma_y}{\text{FOS}} \tag{6}$$

where σ_y is the yield stress and $\text{FOS} = 1.2$ is the applied factor of safety. Thus, we define the objective value as follows:

$$\boldsymbol{\delta} = F_{\text{ext}}{}^{-1}_{(\sigma_{\text{mises}} = \sigma_{\text{lim}})} \tag{7}$$

The external load is applied at an angle of $\varphi = 26.57$ deg, corresponding to a friction coefficient of $\mu = 0.5$ between gripper finger and object.

To obtain feasible designs, geometric constraints are applied that limit the range of feasible design parameters. They ensure that the resulting designs comply to the fundamental topology as shown in Fig. 3 and observe a minimum distance of $\varepsilon = 0.3$ mm between all flexures. To this end, the relative angles have to be in an increasing order such that every $\alpha_i < \alpha_{i+1}$, and the following relationship

has to be observed in order to avoid flexure interference toward the center of the mechanism.

$$\xi \geq 2\left(\arcsin\frac{t}{d} + \arcsin\frac{\varepsilon}{d}\right) \tag{8}$$

where ξ is the smallest angle between any two flexures of the hinge, based on the relative angles α. Thus, this constraint effectively imposes a minimum inner diameter d for any given angles α, flexure thickness t, and minimum distance ε. In addition to these initial checks, all flexures are checked for collisions during simulation. To prevent these, a penalty is added to the objective, which is proportional to the amount of collisions that are detected.

Optimizations are conducted for all configurations $n = [1\ldots8]$ using the *particleswarm()* solver from the MATLAB Global Optimization Toolbox.

2.7 Initial Design Study. To provide insight into the effect of using different numbers n of flexure pivots per hinge half on the range of motion, loadability, and lateral support stiffness of the flexure hinge, SPACAR simulations according to Sec. 2.5 are preformed for all configurations $n = [1\ldots8]$ using a "default" design. In this "default" design, the flexures are equally spaced within each quadrant, as shown in Fig. 3. Thereby, the spacing between the flexures across two adjacent quadrants is effectively doubled, to make the first and last flexure pivot in each half of the hinge less prone to torsion. Furthermore, the minimum thickness $t = 0.3$ mm and minimum inner diameter for d are used to maximize the achievable range of motion. The minimum inner diameter is found by minimizing d in Eq. (8) for given values of t, ε, and ξ, whereby for the "default" designs ξ is a function of n.

2.8 Verification. For verification of the beam-based SPACAR simulations and for comparison with the experimental results, additional static structural simulations are performed in ANSYS. Since the load case used in the experiment differs slightly from the computational model used for optimization, a separate verification model is used (see Fig. 5). This verification model emulates the experiment and is implemented in both SPACAR and ANSYS.

The ANSYS simulations use a detailed model of the entire specimen geometry including the actuation tendon, and investigate two cases. In the first case, the frame, i.e., all parts except the flexures and tendon, are rigid. This corresponds to the SPACAR verification model and is thus expected to yield similar results. In the second case, all parts, including the frame, are flexible. This corresponds to the physical model and is thus used for comparison with the experiment.

3 Experiment

An experiment is performed to characterize the mechanical behavior of a hinge that is designed and optimized according to the synthesis method described in this article. Specifically, the support stiffness in the lateral direction and the actuation force exerted by the tendon are investigated. To this end, a flexure hinge specimen and dedicated test setup are made.

3.1 Specimen. The specimen is shown in Fig. 6. It is a monolithic structure that consists of a fixation block that acts as the fixed shuttle, a lever that acts as the mobile shuttle, and the flexure hinge itself. The fixation block is used to fix the specimen to the test setup using two M3 bolts. The lever is used to apply loads to the hinge and has several features: A ring-shaped section extends along the perimeter of the hinge to the attachment point of the tendon, which is a hole through which the tendon wire is guided and to which it is fixed. At the far end of the lever, another such hole serves as the attachment for a wire from which a weight can be suspended. Its location corresponds to the location at which external loads are applied in simulation. Above and to the side of this hole

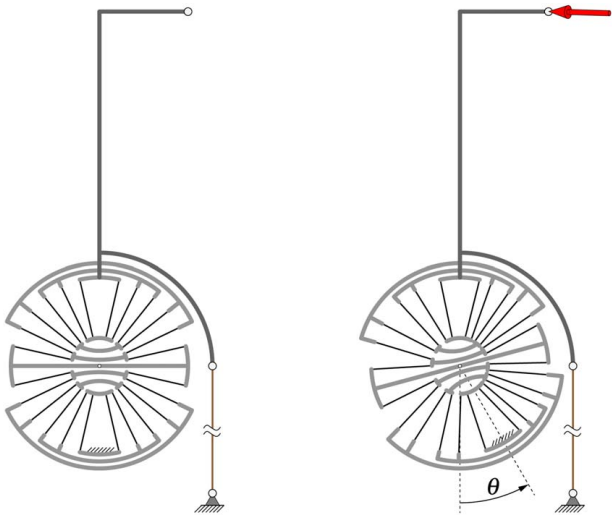

Fig. 5 Verification model. The left subfigure shows the undeformed state before any loads are applied. The right subfigure depicts the two-step loading procedure. In the first step, the fixed shuttle is rotated by an angle θ (= 30 deg) about the joint center, while the load lever is held in place by a tendon, which is fixed to the ground. The resulting load is equivalent to the tendon applying the rotation by pulling at the phalanx. In the second step, the external force F_{ext} is applied at the end of the load lever. The force F_{ext} is indicated by the perspective arrow and has a fixed angle φ toward the drawn x-y plane. In comparison to the optimization model (see Fig. 4), the location at which the load lever is fixed and its constraint direction with respect to the fixed shuttle are rotated by θ about the pivot axis, altering the load case slightly.

are two round surface features to measure displacements using a laser displacement sensor. Cylindrical bars are integrated into the lever to fix the wires to after guiding them through the holes.

The hinge is based on an optimized design consisting of six flexure pivots per hinge half ($n = 6$). The set of optimized parameters is stated in Sec. 4. The first and last flexure pivots of the hinge that act as the input and output are located at the inside and are enclosed by the concentric frames that connect the intermediate flexure pivots (compare Figs. 3 and 6). Bridge features are used to connect these input and output pivots to the fixation block and lever, respectively, which are located outside the flexure hinge. Each bridge forms a 45 deg arch that crosses the two rings-shaped frames in between. To maintain the same width as the flexures, the

Fig. 6 Test specimen containing the optimized flexure hinge ($n = 6$), made by a commercial supplier from a performance grade Ti-6Al-4V alloy [41] via additive manufacturing. Caliper for scale.

frames feature cutouts that enable the lever to pass through and perform its ±30 deg range of motion without collision. Furthermore, the frames are designed such that they do not protrude beyond a diameter of 21.5 mm along the traverse axis. This ensures an air gap of 0.75 mm between the hinge and the tendon wire, which is guided along the outer perimeter with a diameter $D_o = 23$ mm. The tendon wire is made from steel (Young's modulus $E_t \approx 210$ GPa) and has a diameter $d_t = 0.8$ mm.

3.2 Test Setup. Figure 7 shows the test setup. Its frame consists of 40 × 40 mm aluminum profiles and 3 mm steel plate, which are bolted together and fixed to a 25 mm aluminum plate. The specimen is bolted to a rotating platform that shares the same rotation axis as the flexure hinge. An angle scale and an arrow indicator are used to measure the rotation angle of the platform with respect to the frame. The platform can be fixed to the frame by tightening two M6 bolts. A 150 mm long steel wire with 0.8 mm diameter is used as the tendon. It is fixed to the specimen at one end and to a ME-Meßsysteme KM26z load cell at the other end. The load cell is suspended by a plastic bracket and is fixed to the frame via a ball joint. This fixation ensures that the load cell aligns with the force acting along the tendon, without applying its weight onto the tendon. An adjustable weight is suspended from the tip of the specimen lever via another wire to simulate a lateral ($\varphi = 90$ deg) external load. Colinear with the applied external load, a displacement measurement is performed using a Micro-Epsilon Messtechnik optoNCDT 1402-20 laser displacement sensor, which measures the distance from a fixed position on the frame to the round surface feature on the lever.

When a measurement is performed, a rotation is applied to the fixation block of the specimen via the rotating platform. While applying the rotation, the lever is held in place by the tendon. Thus, the deflection of the flexure hinge in its degree-of-freedom corresponds to the rotation angle applied to the platform. The force in the tendon corresponding to the actuation force in a tendon-actuated gripper is measured by the load cell. At every angle, the external load can be varied by adding or removing segments of the suspended adjustable weight. By measuring the applied weight and the lateral displacement, the lateral stiffness of the flexure hinge can be determined at every deflection angle. Due to practical considerations, it was chosen to keep the specimen lever and the sensors that are referencing to it stationary, while the rotation is applied to the fixation block. This is different from the computational model used for optimization in which the lever is rotated, as shown in Fig. 4. To account for this alteration, a separate verification model, shown in Fig. 5, is used for comparison between experimental and computational results.

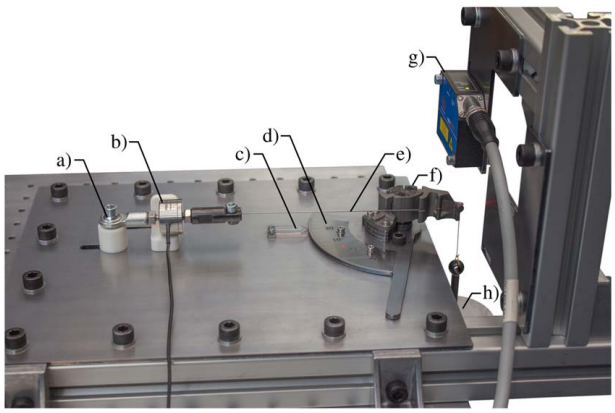

Fig. 7 Test setup with specimen deflected by $\theta = 30$ deg: (a) ball joint, (b) load cell, (c) arrow indicator, (d) rotating platform with angle scale, (e) tendon wire, (f) specimen, (g) laser displacement sensor, and (h) adjustable weight

The measurement data are obtained using a PC with a National Instruments PCI-6221 multifunction I/O card and a National Instruments BNC-2110 adapter. The laser displacement sensor connects to the adapter directly, while the load cell connects via a ME-Meßsysteme GSV-11H 010-5/20/2 measuring amplifier powered by a battery. The PC running SIMULINK REAL-TIME converts the signals and displays them on a monitor. Experiments are performed by suspending a fixed weight from the lever and increasing the rotation angle in steps of 2 deg from −2 deg to 30 deg and vice versa. At each angle, the sensor values displayed on the monitor are logged manually. The data for the actuation force are acquired without applying any weight. The data for the lateral stiffness are acquired using a fixed weight of 1567 g.

4 Results

Figures 8 and 9 show the results of the initial design study described in Sec. 2.7. Figure 8 shows the angle-dependent loadability. For pure lateral loads ($\varphi = 90$ deg), a clear trend can be observed. As the number of flexure pivots increases, the loadability at $\theta = 0$ deg decreases, however maintains a more constant level with increasing rotation. Along with this, a larger range of motion

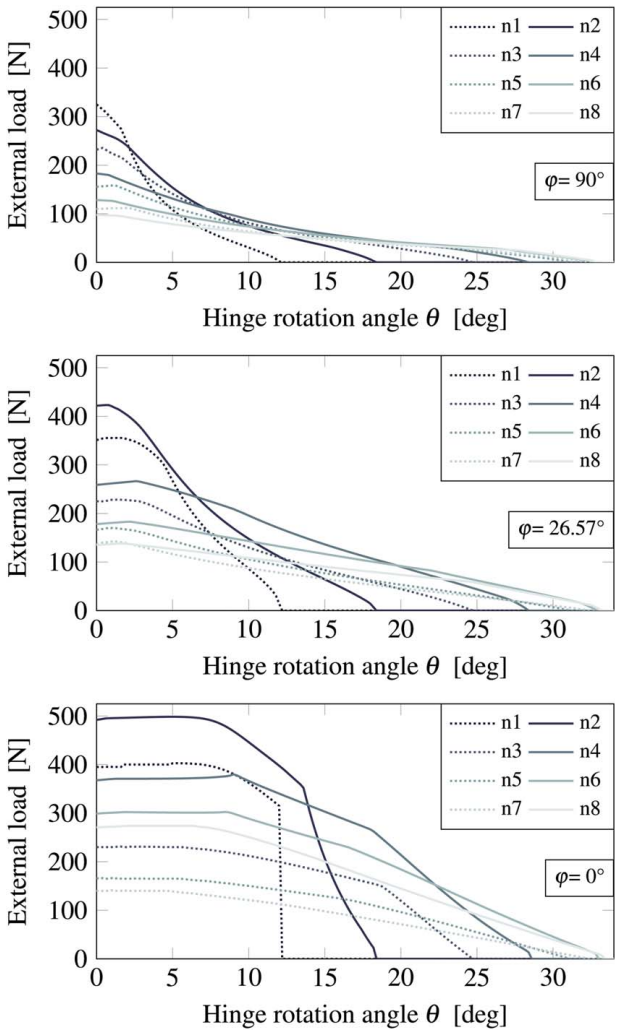

Fig. 8 Loadability of the "default" designs (shown in Fig. 3). The graphs show the external load at which one of the flexures of the respective "default" design exceeds the limit stress $\sigma_{lim} = 750$ MPa in SPACAR (optimization model), depending on the applied rotation θ. Each subfigure shows the results for a different angle φ at which the load is applied. The second subfigure corresponds to the load angle used in optimization ($\mu = 0.5$).

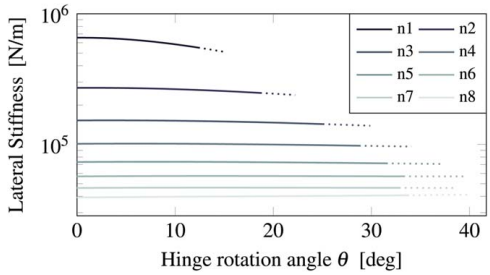

Fig. 9 Lateral support stiffness of the "default" designs (shown in Fig. 3) without external load. The graph shows the lateral stiffness ($\varphi = 90$ deg) at the load application point determined in SPACAR (optimization model) for each "default" design. The solid line shows the stiffness up to the limit stress $\sigma_{\text{lim}} = 750$ MPa, while the dotted line extends until the yield stress $\sigma_{\text{lim}} = 900$ MPa.

is achieved. As the angle φ at which the load is applied is decreased ($\varphi = 26.57$ deg), the loadability increases and remains more steady throughout all design, while the achievable range of motion remains unaffected. Aside from these general trends, though, it can be observed that the gain in loadability is significantly larger for designs with an even number n of flexure pivots per hinge half than those with an odd number. For pure in-plane loads ($\varphi = 0$ deg), the trends continue. In addition, however, plateau-like sections emerge at which the loadability remains near constant at smaller rotation angles.

Figure 9 shows lateral support stiffness of the default designs. It can be seen that the number of employed flexure pivots has a large influence on the lateral stiffness of the hinge, while the stiffness drop is relatively small for all designs throughout their usable range of motion.

Figures 10 and 11 show simulation results of the optimized design. Through multiple optimizations, it is determined that given the geometric constraints, material properties, and applied loads a number of flexure pivots per hinge half of $n = 6$ yields the highest loadability. For $n \leq 4$, no feasible designs are found as the limit stress σ_{lim} even for the minimum flexure thickness of $t = 0.3$ m is already exceeded due to the initially applied rotation. For $n = 5$ and $n \geq 7$, feasible designs are found; however, their loadability turned out lower. These findings correspond to the results of the initial design study, as can be examined in the second graph of Fig. 8. The optimized design has the following design parameters: $\alpha_{1-6} = [20.4,\ 45.1,\ 73.6,\ 98.2,\ 126.8,\ 151.4]$ deg, $d = 4.82$ mm, $t = 0.3$ mm.

Figure 10 shows the loadability of the optimized design across its range of motion for several load application angles ranging from $\varphi = 0$ deg to $\varphi = 90$ deg. Figure 11 shows a comparison of SPACAR and ANSYS. The top graph shows the responses to a 30 deg rotation of the fixation block, without external load. The bottom graph

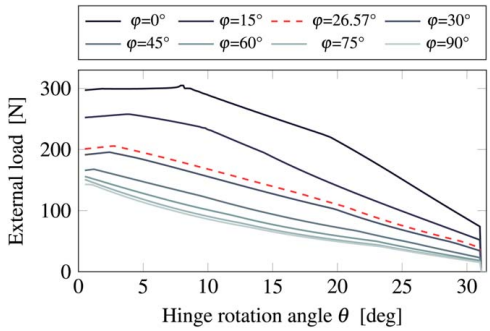

Fig. 10 Loadability of the optimized design ($n = 6$). The graphs show the external load at which one of the flexures exceeds the limit stress $\sigma_{\text{lim}} = 750$ MPa in SPACAR (optimization model), depending on the rotation θ and the angle φ at which the load is applied. The dashed line ($\varphi = 26.57$ deg) indicates the load angle for which the flexure hinge is optimized.

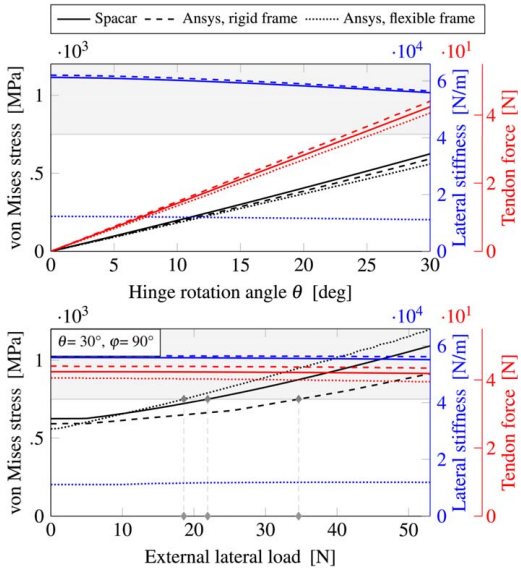

Fig. 11 Comparison between SPACAR (verification model) and ANSYS for the initial hinge rotation without external load (top) and subsequent external lateral loading (bottom). The gray field indicates the region above the limit stress $\sigma_{\text{lim}} = 750$ MPa. Markers show the loadability at the stress limit.

shows the response to a lateral ($\varphi = 90$ deg) external load that is subsequently applied to the lever. It can be seen that during rotation, there is good agreement between all models regarding flexure stresses and the force exerted by the tendon. However, while the ANSYS model with rigid-frame sections shows approximately the same lateral stiffness as the SPACAR model, its fully flexible counterpart shows a significantly lower lateral stiffness. During the subsequent loading, the lateral stiffness and tendon force maintain approximately the same level as at the end of the rotation, while the stresses continue to increase at different rates. Compared with the SPACAR model, the rigid-frame ANSYS model exhibits a more modest increase in stress, leading to higher loadability, while the flexible-frame ANSYS model exhibits a steeper increase in stress, leading to lower loadability.

Figures 12 and 13 show experimental results along with the corresponding flexible-frame ANSYS simulations. It can be seen that both tendon force and the lateral stiffness show a significant deviation between the measurement data and the simulation results when using the original design dimensions. The measured mechanical behavior suggest that the effective wall thickness of the manufactured part is smaller than originally specified. It is found that by removing a uniform layer of 0.0325 mm from all segments of the

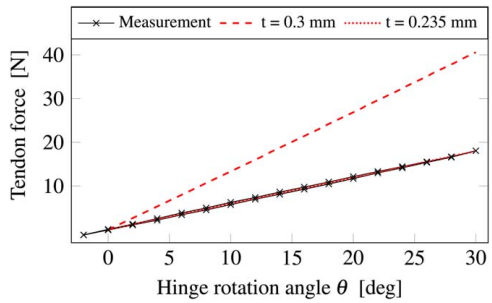

Fig. 12 Tendon force in experiment and simulation. The measurement data are acquired in counterclockwise direction, without external load. The shaded area indicates the enclosed hysteresis field. ANSYS simulation results are shown for original and reduced hinge dimensions, denoted by their respective flexure thicknesses.

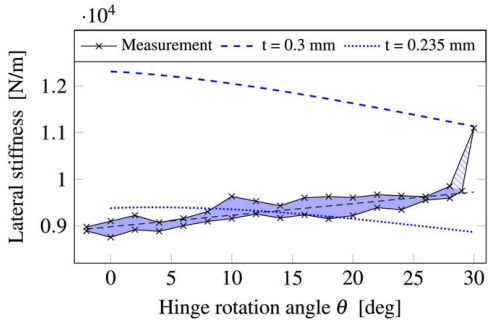

Fig. 13 Lateral support stiffness in experiment and simulation. The measurement data are acquired in clockwise direction while applying a constant external lateral load (at $\varphi = 90$ deg). The shaded area indicates the enclosed hysteresis field. The black dashed line shows a linear fit of the measured data, excluding the measurement at 30 deg. ANSYS simulation results are shown for original and reduced hinge dimensions, denoted by their respective flexure thicknesses.

flexure hinge, resulting in flexure thickness of $t = 0.235$ mm, the simulation yields a tendon force that closely fits the measurement data, as shown in Fig. 12. By removing this layer, also the lateral stiffness matches the measurement more closely, though a significant deviation remains. While the simulation shows a loss of stiffness with increasing rotation, the measurement data appear to indicate an increase in stiffness. At 30 deg, a rapid increase in stiffness is measured, which significantly deviates from the overall trend.

5 Discussion

Increasing the number of flexure pivots generally improves the range of motion and loadability of the flexure hinge at large rotations. However, as can be seen in Fig. 8, these gains are diminishing beyond a certain number of flexure pivots. This can be explained by the relationship stated in Eq. (8). It states that, as the number of flexure pivots increases so must the inner diameter d. Hence, beyond a certain number of flexure pivots, the loss incurred by shortening the flexures outweighs the gain by distributing deformations over multiple flexures. A peculiar effect that can be seen in Fig. 8 is that in the presence of significant in-plane loads ($\varphi << 90$ deg) hinges with an odd number of flexure pivots per hinge half perform worse in terms of loadability than those with an even number. This inherently makes them the worse choice for grippers and many other applications. The plateau-like sections in loadability toward lower angles for pure in-plane loads ($\varphi = 0$ deg), shown in the same figure, may point toward a failure caused by buckling. As shown in Fig. 9, increasing the number of flexure pivots has a drastic decreasing effect on the lateral support stiffness of the hinge. However, all investigated flexure hinges—both in simulation and experiment—maintain ample stiffness for the proposed gripper application. Furthermore, the flexure hinges are mainly limited by the stiffness of the frame sections, as illustrated in Fig. 11. Apart from the investigated metrics, the apparent low pivot shift points to another potentially interesting feature of this flexure hinge architecture.

Overall, the data shown in Figs. 8 and 9 provide a concise overview about the effects of using different numbers of flexure pivots for flexure hinges sharing the same design constraints. However, due to the simplification of using rigid-frame sections in the SPACAR simulations, the achievable loadability and lateral support stiffness values will be distinctly lower in practice. Figure 11 shows that, while for the assumption of rigid-frame sections, SPACAR provides sufficiently accurate results, incorporating flexible frames into the model decreases loadability and especially lateral support stiffness significantly. This shows that frames and the design thereof have a substantial influence on the overall performance and should be a focus of attention in future designs. ANSYS simulations of a later redesigns of the tested specimen revealed that by optimizing the frame within the design constraints set in Sec. 2.1, the lateral support stiffness could be approximately doubled and loadability slightly increased. Key areas of improvement concerned increasing the thickness of the concentric frames and increasing the cross section of the bridge arches.

Since determining stresses in experiment is impractical, stiffness properties are used to verify the computational results. When compared to simulations, the experimental results suggest that the physical specimen does not fully correspond to its intended geometry. According to Wei et al. [49], the effective thickness of flexure hinges made via metal additive manufacturing is reduced by a porous layer that corresponds in thickness to the average powder particle diameter. While this average diameter is unknown for the given material, the layer of 32.5 μm, which was removed to match the experimental data, falls in between the specified roughness values of $R_a = 20$ μm and $R_z = 80$ μm [41]. Future designs may be improved by accounting for this effect. Apart from this, the specimen required extensive postprocessing as caked powder had to be removed from small gaps between flexures and frame parts. Minimizing these areas and increasing distances between features will certainly aid manufacturability. The sudden increase in lateral stiffness at 30 deg rotation, shown in Fig. 13, was reproducible and is likely caused by internal contact.

6 Conclusion

The flexure architecture proposed in this article provides a clear framework to design well-performing flexure hinges, in particular for applications in which the designer has to observe challenging constraints with respect to size, material, and manufacturing. By adjusting the number of flexure pivots per hinge half, an optimal trade-off between range of motion, loadability, and stiffness properties can be found that best suit a specific application. This is demonstrated based on the design of a flexure hinge for a compact anthropomorphic gripper made via conventional metal additive manufacturing. For this use case, a dedicated optimization procedure is developed. It allows to maximize the loadability of the hinge when deflected to a specified rotation angle and subject to loads that are representative for use in a tendon-driven gripper. The result is a compact flexure hinge that features a range of motion of ±30 deg. For the range of 0–30 deg, simulations show a lateral loadability of 52.5–18.6 N and lateral support stiffness of 12,309–11,130 N/m, determined at a gripper interface which is located at a distance of 41.2 mm from the pivot axis. A dedicated experiment which is performed confirmed a loadability of at least 15.4 N and determined a stiffness of 8982–9727 N/m for the same conditions.

The results show that the flexure hinge architecture has large potential for a wide range of applications, while in combination with the optimization procedure, superior designs for tendon-driven grippers can be obtained.

Funding Data

- University of Twente under the Strategic Impulse Programme "Human-Centred Robotics."
- Dutch Research Council (NWO) under the research programme P17-01 "FlexCRAFT."

Conflict of Interest

There are no conflicts of interest.

Data Availability Statement

The datasets generated and supporting the findings of this article are obtainable from the corresponding author upon reasonable request.

References

[1] Wolf, A., and Schunk, H., 2018, *Grippers in Motion*, Vol. 5, Carl Hanser Verlag, München.

[2] Chua, P. Y., Ilschner, T., and Caldwell, D. G., 2003, "Robotic Manipulation of Food Products—A Review," Industrial Robot, **30**(4), pp. 345–354.

[3] Blanes, C., Mellado, M., Ortiz, C., and Valera, A., 2011, "Review. Technologies for Robot Grippers in Pick and Place Operations for Fresh Fruits and Vegetables," Spanish J. Agric. Res., **9**(4), pp. 1130–1141.

[4] Bac, C. W., van Henten, E. J., Hemming, J., and Edan, Y., 2014, "Harvesting Robots for High-Value Crops: State-of-the-Art Review and Challenges Ahead," J. Field Rob., **31**(6), pp. 888–911.

[5] Monkman, G. J., Hesse, S., Steinmann, R., and Schunk, H., 2007, *Robot Grippers*, Wiley-VCH Verlag, Weinheim.

[6] Hugo, P., 2013, *Industrial Grippers: State-of-the-Art and Main Design Characteristics*, Springer, London, pp. 107–131.

[7] Lundström, G., 1974, "Industrial Robot Grippers," Ind. Robot, **1**(2), pp. 72–82.

[8] Chen, F., 1982, "Gripping Mechanisms for Industrial Robots: An Overview," Mech. Mach. Theory., **17**(5), pp. 299–311.

[9] Pio Belfiore, N., and Pennestrì, E., 1997, "An Atlas of Linkage-Type Robotic Grippers," Mech. Mach. Theory., **32**(7), pp. 811–833.

[10] Boubekri, N., and Chakraborty, P., 2002, "Robotic Grasping: Gripper Designs, Control Methods and Grasp Configurations—A Review of Research," Integrated Manuf. Syst., **13**(7), pp. 520–531.

[11] Ozawa, R., and Tahara, K., 2017, "Grasp and Dexterous Manipulation of Multi-Fingered Robotic Hands: A Review From a Control View Point," Adv. Rob., **31**(19–20), pp. 1030–1050.

[12] Navas, E., Fernández, R., Sepúlveda, D., Armada, M., and Gonzalez-de Santos, P., 2021, "Soft Grippers for Automatic Crop Harvesting: A Review," Sensors, **21**(8), p. 2689.

[13] Howell, L. L., 2001, *Compliant Mechanisms*, John Wiley & Sons, Inc., New York.

[14] Martin, J., Huard, B., Robert, M., and Grossard, M., 2011, "Novel Self-Sensing Actuated Joint for Robotic Hands," 2011 IEEE/ASME International Conference on Advanced Intelligent Mechatronics (AIM), Budapest, Hungary, July 3–7, pp. 475–480.

[15] Martin, J., Huard, B., Robert, M., and Grossard, M., 2011, "Robotic Hands: Mechatronic Design and Compliance Control of a Self-Sensing Finger Prototype," Computer Methods Biomechan. Biomed. Eng., **14**(S1), pp. 103–105.

[16] Belzile, B., and Birglen, L., 2017, "Optimal Design of Self-Adaptive Fingers for Proprioceptive Tactile Sensing," ASME J. Mech. Rob., **9**(5), p. 051004.

[17] Henein, S., Spanoudakis, P., Droz, S., Myklebust, L. I., and Onillon, E., 2003, "Flexure Pivot for Aerospace Mechanisms," Proceedings of the 10th ESMATS (ESA SP-524), San Sebastian, Spain, Sept. 24–26, pp. 285–288.

[18] Blanding, D., 1999, *Exact Constraint: Machine Design Using Kinematic Principles*, ASME Press, New York.

[19] Smith, S. T., 2000, *Flexures: Elements of Elastic Mechanisms*, CRC Press, Boca Raton, FL.

[20] Howell, L. L., Magleby, S. P., and Olsen, B. M., 2013, *Handbook of Compliant Mechanisms*, John Wiley & Sons, Ltd, Chichester, UK.

[21] Lobontiu, N., 2021, *Compliant Mechanisms: Design of Flexure Hinges*, 2nd ed., CRC Press, Boca Raton, FL.

[22] Odhner, L. U., Jentoft, L. P., Claffee, M. R., Corson, N., Tenzer, Y., Ma, R. R., Buehler, M., Kohout, R., Howe, R. D., and Dollar, A. M., 2014, "A Compliant, Underactuated Hand for Robust Manipulation," Int. J. Robot. Res., **33**(5), pp. 736–752.

[23] Lotti, F., and Vassura, G., 2002, "A Novel Approach to Mechanical Design of Articulated Fingers for Robotic Hands," IEEE/RSJ International Conference on Intelligent Robots and Systems, Lausanne, Switzerland, Sept. 30–Oct. 4, Vol. 2, pp. 1687–1692.

[24] Berselli, G., Parvari Rad, F., Vertechy, R., and Parenti Castelli, V., 2013, "Comparative Evaluation of Straight and Curved Beam Flexures for Selectively Compliant Mechanisms," 2013 IEEE/ASME International Conference on Advanced Intelligent Mechatronics, Wollongong, Australia, July 9–12, pp. 1761–1766.

[25] Dollar, A. M., and Howe, R. D., 2007, "The SDM Hand as a Prosthetic Terminal Device: A Feasibility Study," 2007 IEEE 10th International Conference on Rehabilitation Robotics, Noordwijk, The Netherlands, June 12–15, pp. 978–983.

[26] Ma, R. R., Odhner, L. U., and Dollar, A. M., 2013, "A Modular, Open-Source 3D Printed Underactuated Hand," 2013 IEEE International Conference on Robotics and Automation, Karlsruhe, Germany, May 6–10, pp. 2737–2743.

[27] Mutlu, R., Alici, G., and Spinks, G., 2015, "Effect of Flexure Hinge Type on a 3D Printed Fully Compliant Prosthetic Finger," 2015 IEEE International Conference on Advanced Intelligent Mechatronics (AIM), Busan, South Korea, July 7–11, pp. 790–795.

[28] Hill, S., and Canfield, S., 2016, "An Assessment of Fused Deposition Modeling for the Manufacturing of Flexural Pivots in an Anthropomorphic Robotic Hand Design," Proceedings of the ASME 2016 International Design Engineering Technical Conferences and Computers and Information in Engineering Conference, Vol. Volume 5B: 40th Mechanisms and Robotics Conference, Charlotte, NC, Aug. 21–24, Paper No. DETC2016-60253.

[29] Lotti, F., Tiezzi, P., Vassura, G., Biagiotti, L., Palli, G., and Melchiorri, C., 2005, "Development of UB Hand 3: Early Results," Proceedings of the 2005 IEEE International Conference on Robotics and Automation, Barcelona, Spain, Apr. 18–22, pp. 4488–4493.

[30] Berselli, G., Piccinini, M., and Vassura, G., 2011, "Comparative Evaluation of the Selective Compliance in Elastic Joints for Robotic Structures," 2011 IEEE International Conference on Robotics and Automation, Shanghai, May 9-13.

[31] Tavakoli, M., and de Almeida, A. T., 2014, "Adaptive Under-Actuated Anthropomorphic Hand: ISR-SoftHand," 2014 IEEE/RSJ International Conference on Intelligent Robots and Systems, Chicago, IL, Sept. 14–18, pp. 1629–1634.

[32] Tavakoli, M., Batista, R., and Sgrigna, L., 2016, "The UC Softhand: Light Weight Adaptive Bionic Hand With a Compact Twisted String Actuation System," Actuators, **5**(1), p. 1.

[33] Tavakoli, M., Sayuk, A., Lourenço, J., and Neto, P., 2017, "Anthropomorphic Finger for Grasping Applications: 3D Printed Endoskeleton in a Soft Skin," Int. J. Adv. Manuf. Technol., **91**(5), pp. 2607–2620.

[34] Martin, J., and Robert, M., 2010, "Novel Flexible Pivot With Large Angular Range and Small Center Shift to Be Integrated Into a Bio-Inspired Robotic Hand," Proceedings of the ASME 2010 Conference on Smart Materials, Adaptive Structures and Intelligent Systems, Philadelphia, PA, Sept. 28–Oct. 1, ASME , Vol. 2, pp. 427–431.

[35] Martin, J., and Robert, M., 2011, "Novel Flexible Pivot With Large Angular Range and Small Center Shift to Be Integrated Into a Bio-Inspired Robotic Hand," J. Intell. Material Syst. Struct., **22**(13), pp. 1431–1437.

[36] Garcia, L., Naves, M., and Brouwer, D., 2018, "3D-Printed Flexure-Based Finger Joints for Anthropomorphic Hands," 2018 IEEE/RSJ International Conference on Intelligent Robots and Systems (IROS), Madrid, Oct. 1–5.

[37] Boers, B., Naves, M., Garcia, L., and Brouwer, D. M., 2018, "Inverted Curved Flexure Hinge With Torsional Reinforcements in a Printed Prosthetic Finger," Proceedings of the 33rd ASPE Annual Meeting 2018, Las Vegas, NV, Nov. 4 – 9, pp. 582–587.

[38] Tilley, A. R., 2001, *The Measure of Man and Woman: Human Factors in Design, Revised Edition*, Vol. 12, Whitney Library of Design, New York.

[39] Hume, M. C., Gellman, H., McKellop, H., and Brumfield Jr., R. H., 1990, "Functional Range of Motion of the Joints of the Hand," J. Hand Surgery, **15**(2), pp. 240–243.

[40] Bain, G. I., Polites, N., Higgs, B. G., Heptinstall, R. J., and McGrath, A. M., 2015, "The Functional Range of Motion of the Finger Joints," J. Hand Surgery (European Volume), **40**(4), pp. 406–411.

[41] Materialise, N. V., 2021, *Datasheets 3D Printing Materials*, Vol. 6, Materialise NV, Leuven.

[42] Bartsch, K., Herzog, D., Bossen, B., and Emmelmann, C., 2021, "Material Modeling of Ti–6Al–4V Alloy Processed by Laser Powder Bed Fusion for Application in Macro-scale Process Simulation," Mater. Sci. Eng. A., **814**, p. 141237.

[43] Wu, Z., Narra, S. P., and Rollett, A., 2020, "Exploring the Fabrication Limits of Thin-Wall Structures in a Laser Powder Bed Fusion Process," Int. J. Adv. Manuf. Technol., **110**(1), pp. 191–207.

[44] Kranz, J., Herzog, D., and Emmelmann, C., 2015, "Design Guidelines for Laser Additive Manufacturing of Lightweight Structures in TiAl6V4," J. Laser. Appl., **27**(S1), p. S14001.

[45] Thomas, D. J., 2009, *The Development of Design Rules for Selective Laser Melting*, University of Wales Institute, Cardiff, UK.

[46] Pei, X., Yu, J., Zong, G., Bi, S., and Hu, Y., 2009, "A Novel Family of Leaf-Type Compliant Joints: Combination of Two Isosceles-Trapezoidal Flexural Pivots," ASME J. Mech. Rob., **1**(2), p. 021005.

[47] Pei, X., Yu, J., Zong, G., and Bi, S., 2012, "A Family of Butterfly Flexural Joints: Q-LITF Pivots," ASM J. Mech. Des., **134**(12), p. 121001.

[48] Jonker, J. B., and Meijaard, J. P., 1990, *SPACAR—Computer Program for Dynamic Analysis of Flexible Spatial Mechanisms and Manipulators*, Springer Berlin Heidelberg, Berlin/ Heidelberg, pp. 123–143.

[49] Wei, H., Shirinzadeh, B., Niu, X., Zhang, J., Li, W., and Simeone, A., 2021, "Study of the Hinge Thickness Deviation for a 316L Parallelogram Flexure Mechanism Fabricated via Selective Laser Melting," J. Intell. Manuf., **32**(5), pp. 1411–1420.